

1      ***Phytophthora palmivora establishes tissue-specific intracellular infection***  
2      ***structures in the earliest divergent land plant lineage***

3      **Short Title:** Haustoria-like Phytophthora Structures in Liverwort Cells

4  
5      **Authors:** Philip Carella, Anna Gogleva, Marta Tomaselli, Carolin Alfs, Sebastian  
6      Schornack\*

7  
8      Sainsbury Laboratory, University of Cambridge, Cambridge, United Kingdom.

9      **\*Corresponding Author:** Sebastian Schornack (sebastian.schornack@slcu.cam.ac.uk)

10  
11     **ABSTRACT**

12     The expansion of plants onto land was a formative event that brought forth profound  
13     changes to the Earth's geochemistry and biota. Filamentous eukaryotic microbes  
14     developed the ability to colonize plant tissues early during the evolution of land  
15     plants, as demonstrated by intimate symbiosis-like associations in >400 million-year-  
16     old fossils. However, the degree to which filamentous microbes establish pathogenic  
17     interactions with early divergent land plants is unclear. Here, we demonstrate that  
18     the broad host-range oomycete pathogen *Phytophthora palmivora* colonizes  
19     liverworts, the earliest divergent land plant lineage. We show that *P. palmivora*  
20     establishes a complex tissue-specific interaction with *Marchantia polymorpha*, where  
21     it completes a full infection cycle within air chambers of the dorsal photosynthetic  
22     layer. Remarkably, *P. palmivora* invaginates *M. polymorpha* cells with haustoria-like  
23     structures that accumulate host cellular trafficking machinery and the membrane-  
24     syntaxin MpSYP13B but not the related MpSYP13A. Our results indicate that the  
25     intracellular accommodation of filamentous microbes is an ancient plant trait that is  
26     successfully exploited by pathogens like *P. palmivora*.

27  
28     **KEY WORDS:** Bryophyte, Biotrophy, Haustoria, Liverworts, *Marchantia polymorpha*,  
29     Oomycetes, *Phytophthora*, Syntaxin

32 **ABBREVIATIONS:** DEG, differentially expressed genes; DPI, days post inoculation;  
33 LFC, log fold change; FDR, false discovery rate; ORF, open reading frame; NPP,  
34 necrosis inducing *Phytophthora* protein; SCR, small cysteine-rich peptides; CWDE,  
35 cell wall degrading enzyme; PI, protease inhibitor; EPI, extracellular protease  
36 inhibitor; TM, transmembrane domain; SP, signal peptide; SYP, syntaxin

37

38 **INTRODUCTION**

39 Plant-microbe associations are ubiquitous throughout the plant kingdom,  
40 which suggests that the ability to support microbial colonization occurred early during  
41 the evolution of land plants. Extensive evidence reveals that the first land plants  
42 were colonized by filamentous eukaryotic microbes, as several fossils from the  
43 Rhynie Chert (Early Devonian, 400-480 MYA) contain symbiosis-like microbial  
44 structures within ancient plant cells [1-4]. Indeed, symbiotic interactions with  
45 arbuscular mycorrhizal fungi are widespread among extant early land plants [5-8].  
46 Moreover, recent studies suggest that early land plants and their algal predecessors  
47 were pre-adapted for symbiosis, as these organisms encode functionally equivalent  
48 homologs of core symbiosis signaling components [9,10]. In comparison, our  
49 understanding of how early divergent land plants interact with pathogenic microbes  
50 remains extremely limited.

51

52 Interactions between plants and filamentous eukaryotic microbes are often  
53 associated with the development of specialized microbial structures that protrude  
54 into plant cells. Such structures include finely-branched arbuscules of symbiotic  
55 arbuscular mycorrhizal fungi and digit, knob, or peg-like haustoria of oomycete and  
56 fungal pathogens [11,12]. Arbuscules and haustoria are both involved in the  
57 manipulation of host cell function to improve microbial colonization, however,  
58 symbiotic structures participate in the mutually beneficial exchange of resources  
59 while pathogenic structures function to suppress host immune responses and  
60 remove nutrients from the host [13,14]. Numerous host tissues and cells are capable  
61 of supporting filamentous microbes [13,15,16], which suggests that partially  
62 overlapping mechanisms are employed to accommodate symbiotic and pathogenic  
63 microbes. This has led to the idea that pathogens establish intracellular interfaces by  
64 exploiting host machinery designed to accommodate endosymbiotic structures.

65 Whether this dynamic was established early during the co-evolution of plants and  
66 microbes is unknown. Extensive evidence has demonstrated that early land plants  
67 can accommodate arbuscules within their cells [7], whereas specialized pathogenic  
68 structures like haustoria have not been observed in these plants.

69

70 Bryophytes are a basal group of nonvascular, gametophyte-dominant  
71 (haploid) early land plants that include liverworts, hornworts, and mosses.  
72 Phylogenetic analyses often place liverworts basal to mosses and hornworts  
73 [17,18]. This suggests that liverworts represent the earliest divergent land plant  
74 lineage, although this has yet to yield a consensus among the field [19,20]. Many  
75 bryophytes are colonized by symbiotic microbes, however intracellular  
76 endosymbiotic structures (arbuscules) have only been observed in liverworts and  
77 hornworts [7,18]. Unfortunately, our understanding of plant-pathogen interactions in  
78 these plants is extremely limited. In comparison, several groups have described  
79 pathogenic interactions in the model moss *Physcomitrella patens* [21-23]. The  
80 colonization of moss tissues is associated with intracellular hyphal growth, however  
81 specialized infection structures similar to haustoria are not observed within moss  
82 cells [22]. An alternative bryophyte model system is therefore required to study  
83 intracellular interactions with pathogenic microbes. Liverworts are the most suitable  
84 candidate to accomplish this, given their ability to accommodate endosymbiotic  
85 structures and the recent establishment of molecular genetic tools in these plants  
86 [24].

87

88 In this study, we investigated plant-pathogen interactions in the model  
89 liverwort *Marchantia polymorpha*, which propagates clonally via small propagules  
90 (gemmae) or sexually when the sperm of male plants fertilize eggs housed in the  
91 archegonia of female plants. Both male and female plants have a thalloid body plan  
92 comprised of a ventrally located epidermis with rhizoids and scales, a central non-  
93 photosynthetic storage region, and a dorsal photosynthetic layer [25]. The  
94 photosynthetic layer of complex liverworts like *M. polymorpha* is made up of air  
95 chambers, which are walled enclosures that contain plastid-rich photosynthetic  
96 filaments and have open pores to facilitate gas exchange [25].

97

98 To determine if liverworts support intracellular colonization by a filamentous  
99 eukaryotic pathogen, we challenged *M. polymorpha* with *Phytophthora palmivora*, a  
100 broad host-range hemi-biotrophic oomycete pathogen with demonstrated virulence in  
101 root and leaf tissues of monocot and dicot hosts [26-28]. In general, *P. palmivora*  
102 infection begins when motile zoospores contact plant surfaces, causing the spores to  
103 encyst, germinate and form appressoria to penetrate the surface [29]. Upon  
104 accessing plant tissues, the biotrophic phase of *P. palmivora* colonization begins and  
105 the pathogen develops digit-like haustoria that protrude into plant cells for nutrient  
106 acquisition and the release of virulence effector proteins that manipulate the host  
107 [11]. Precise mechanisms for oomycete effector delivery/uptake remain to be  
108 clarified, however secreted effector proteins containing the RXLR motif translocate  
109 into host cells and interfere with immunity [30-32]. The pathogen eventually  
110 transitions to a necrotrophic phase, where it actively destroys plant tissues and  
111 completes its asexual lifestyle by releasing motile zoospores contained within  
112 sporangia [33].

113

114 Here, we demonstrate that *P. palmivora* preferentially colonizes the  
115 photosynthetic layer of liverworts and causes extensive disease. Molecular and  
116 microscopic analyses revealed that the biotrophic phase of *P. palmivora* colonization  
117 is associated with the upregulation of virulence effector molecules and the  
118 deployment of haustoria-like intracellular infection structures. Several endogenous  
119 host proteins accumulated at intracellular infection structures, including Rab  
120 GTPases and the homolog of a membrane-localized syntaxin associated with  
121 symbiosis in higher plants. Together, these markers clearly defined atypically  
122 branched infection structures and intracellular hyphae, revealing a prevalent  
123 intracellular phase of *P. palmivora* pathogenesis that is not commonly observed  
124 during interactions with higher plants. Furthermore, we demonstrate that *P.*  
125 *palmivora* requires liverwort air chambers to fully exploit *M. polymorpha*, as pathogen  
126 fitness is greatly reduced in air chamber-less *nop1* mutants.

127

## 128 **RESULTS**

129

130 ***Phytophthora palmivora* colonizes the photosynthetic layer of**  
131 ***Marchantia polymorpha***

132 To determine whether liverworts support colonization by a broad host-range  
133 filamentous pathogen, we challenged 3-week-old *M. polymorpha* TAK1 (male) plants  
134 with zoospores of a tdTomato-expressing isolate of *P. palmivora* (accession P3914,  
135 derived from Arizona, U.S.A; ARI-td) and tracked pathogen growth and disease  
136 progression. Since *P. palmivora* colonizes multiple tissue types in higher plants  
137 [27,28,34], initial experiments were performed to determine whether colonization  
138 occurs in rhizoids or thalli of *Marchantia*. Rhizoid inoculations led to variable disease  
139 phenotypes, such that plants occasionally exhibited disease symptoms by 7 days  
140 post inoculation (dpi; Fig S1A). Confocal fluorescence microscopy indicated that  
141 rhizoids were mostly devoid of intracellular *P. palmivora* (ARI-td) growth, with rare  
142 instances of intracellular hyphae in damaged rhizoids (Fig S1B). In contrast,  
143 *Marchantia* thalli inoculated with ARI-td zoospores exhibited disease symptoms that  
144 increased in severity from 3-7 dpi (Fig 1A). Epifluorescence and confocal microscopy  
145 supported these observations, demonstrating the gradual spread of ARI-td hyphae  
146 across TAK1 thalli from 1-4 dpi (Fig 1B, Fig S2). Plants were completely colonized  
147 by 7 dpi, demonstrating that *M. polymorpha* thalli are highly susceptible to *P.*  
148 *palmivora*.

149

150 Confocal fluorescence microscopy demonstrated that *P. palmivora* colonized  
151 the surface of *M. polymorpha* thalli in a discrete manner that overlapped with air  
152 chamber morphology (Fig S2). We therefore analyzed cross sections of infected *M.*  
153 *polymorpha* thalli, which revealed high levels of colonization within air chambers at 7  
154 dpi (Fig 1C). Pathogen growth was largely limited to the photosynthetic layer,  
155 although intercellular hyphae were observed in the non-photosynthetic storage tissue  
156 of plants with ongoing necrosis (Fig S3). In support of these findings, experiments  
157 performed using additional liverwort species (*Lunularia cruciata* and *M. paleacea*)  
158 similarly exhibited colonization within air chambers (Fig S4A). Cryo-SEM (scanning  
159 electron microscopy) of colonized *Marchantia* thalli demonstrated *P. palmivora*  
160 sporangia and hyphae traversing through the central pores of air chambers (Fig 1D)  
161 and hyphal growth was observed within air chambers (Fig 1D and 1E). *P. palmivora*  
162 hyphae often associated with photosynthetic filament cells and were sometimes

163 observed to penetrate them (Fig 1E). Together, our results indicate that *P. palmivora*  
164 preferentially colonizes the air chambers of *M. polymorpha*.

165

166 Natural diversity of pathogen isolates has classically been used to probe host-  
167 microbe interactions to identify loci or mechanisms important for plant resistance to  
168 disease. To explore this paradigm in *Marchantia*, we assessed the ability of several  
169 *P. palmivora* isolates to colonize TAK1 thalli (Fig S5). Disease progression was  
170 similar to ARI-td for the majority of strains tested, with the exception of the MAZI  
171 (P6375, Malaysia) and TAZI (P6802, Thailand) isolates that displayed an  
172 accelerated disease progression (Fig S5). We also tested compatibility between  
173 *Marchantia* and *P. infestans*, the causal agent of potato and tomato late blight. TAK1  
174 thalli infected with *P. infestans* (Pi-88069-td) were asymptomatic over a 7-day  
175 infection time course, similar to mock-treated plants (Fig S6). In contrast, TAK1 thalli  
176 inoculated with *P. palmivora* (ARI-td) zoospores were highly susceptible to pathogen  
177 ingress. These results demonstrate that *P. infestans* is unable to overcome pre-  
178 existing or induced barriers to colonization in *Marchantia*, unlike several *P. palmivora*  
179 isolates that cause extensive disease.

180

181 ***P. palmivora* establishes a biotrophic interaction with host-intracellular**  
182 **oomycete hyphae**

183 The colonization of higher plant tissues by *P. palmivora* is associated with  
184 distinct transitions in pathogen lifestyle. These transitions are typically characterized  
185 by the presence of specialized penetration/infection structures and clear shifts in the  
186 *P. palmivora* transcriptome [28]. We first performed confocal fluorescence  
187 microscopy to document the pathogen lifestyle transitions that occur during the  
188 colonization of TAK1 thalli (Fig 2A). At 1 dpi, hyphae of germinated zoospores  
189 appeared to wander along the surface of the thallus without developing appressorial  
190 penetration structures (Fig 1B, Fig 2A, Fig S2). The colonization of plant tissues  
191 occurred by 2 dpi and was associated with the development of biotrophic intracellular  
192 infection structures. We observed typical digit-like haustoria, however, highly  
193 branched intracellular structures and intracellular hyphae were observed in greater  
194 abundance (Fig 2A). For every digit-like haustorium, there were approximately four  
195 times as many branched intracellular structures and twice as many instances of

196 intracellular hyphal growth. Intracellular structures were also observed during  
197 interactions with *L. cruciata* and *M. paleacea*, however digit or knob-like haustoria  
198 appeared to be more prevalent than branched infection structures (Fig S4B).  
199 Sporangia were observed by 3-4 dpi (Fig 2A), indicating that *P. palmivora* completes  
200 a full infection cycle in *Marchantia*.

201

202 To further clarify the timing of pathogen lifestyle transitions during the  
203 *Marchantia-Phytophthora* interaction, we monitored the expression of lifestyle-  
204 associated *P. palmivora* marker genes over a four-day infection time course by qRT-  
205 PCR analysis (Fig 2B). Levels of the *P. palmivora* biomass marker *PpEF1a*  
206 significantly increased over time, which is consistent with our microscopic analyses  
207 (Fig 1B, Fig S2). The biotrophy-specific marker gene *PpHmp1* (*Haustoria Membrane*  
208 *Protein1* [35]) peaked in expression at 2 dpi, while the sporulation-specific cell cycle  
209 marker gene *PpCdc14* [36] was induced by 3-4 dpi. These results are consistent with  
210 our microscopy data that demonstrates intracellular infection structures at 2 dpi and  
211 sporangia at 3-4 dpi (Fig 2A). Collectively, our results indicate that the *P. palmivora*  
212 infection cycle in *Marchantia* begins with spore germination and hyphal growth at 1  
213 dpi, followed by a biotrophic phase that includes intracellular infection structures at 2-  
214 3 dpi, and ends with the completion of the pathogen's asexual life-cycle after 3 dpi.

215

216 The transcriptional induction of pathogen genes encoding secreted effector  
217 proteins is a hallmark of *Phytophthora*-angiosperm interactions. Among these  
218 secreted proteins, the RXLR class of effectors are believed to act within host cells to  
219 suppress immunity and enhance pathogen growth [30-32]. To determine if *P.*  
220 *palmivora* upregulates RXLR effectors during the colonization of *Marchantia*, we  
221 analyzed the expression profiles of the *P. palmivora* RXLR effectors *REX1*, *REX3*,  
222 and *REX4* [28]. Significant upregulation of *REX1* transcripts occurred during the  
223 biotrophic phase at 2 dpi and *REX3* levels increased throughout infection to a  
224 maximum observed at 4 dpi (Fig 2C). *REX4* expression peaked at 2 dpi, although  
225 this was not statistically significant in all experiments. *REX* expression profiles were  
226 similar to those observed in colonized *N. benthamiana* roots [28], demonstrating that  
227 *P. palmivora* upregulates RXLR effector transcripts during the colonization of  
228 *Marchantia* thalli.

229

230 In order to assess broad transcriptional changes in *P. palmivora* during  
231 liverwort colonisation, we performed RNA-sequencing of infected thalli (3 and 4 dpi)  
232 and axenically grown *P. palmivora* mycelia, which served as an *ex planta* control.  
233 Differential expression analysis revealed 3601 up-regulated and 932 down-regulated  
234 *P. palmivora* genes expressed *in planta* relative to the *ex-planta* control (absolute  
235 LFC  $\geq 2$ , adjusted *p-value*  $< 10^{-3}$ ) (Fig 2D; Table S1). qRT-PCR analysis validated a  
236 subset of colonization-induced *P. palmivora* genes, which were either upregulated  
237 throughout colonization or were induced late during infection (Fig S7). Amongst all  
238 up-regulated genes, 394 (11%) were predicted to encode putative secreted proteins  
239 with RXLR effectors and cell wall degrading enzymes being the most abundant  
240 functional categories (Fig 2E). Taken together these results suggest that *P.*  
241 *palmivora* infection of *M. polymorpha* involves large-scale transcriptional induction of  
242 genes typical of a compatible interaction, including effectors and hydrolytic enzymes.  
243

#### 244 **Host Cellular Responses to Intracellular Infection Structures**

245 The accommodation of intracellular hyphal structures requires reorganization  
246 of the host cell and the biogenesis of novel membranes to separate the host cell  
247 from the pathogen. Moreover, plants responding to invading microbes often  
248 accumulate callose, a  $\beta$ -1,3-glucan associated with cell wall strengthening. We  
249 therefore applied callose staining and live-cell imaging of fluorescently tagged  
250 proteins labelling membrane compartments to investigate the subcellular changes  
251 associated with accommodating intracellular *P. palmivora* structures in *Marchantia*.  
252 An extended callosic envelope is characteristic of dysfunctional intracellular  
253 structures while functional interfaces display callosic collars that are limited to the  
254 neck region or no callosic depositions at all [37,38]. Aniline blue staining of ARI-td-  
255 infected TAK1 thalli revealed that callose deposition was limited to the peripherally-  
256 located neck region of intracellular infection structures (Fig 3A, Fig S8), suggestive of  
257 functional *P. palmivora*-*Marchantia* interfaces. Next, we localized homologs of host  
258 Rab GTPases that label oomycete haustoria in higher plants and are believed to  
259 direct vesicle delivery to host-pathogen interfaces [39]. We generated transgenic  
260 plants that constitutively overexpress mCitrine-MpRabG3c or mCitrine-MpRabA1e,  
261 since these proteins strongly localize to *P. infestans* haustoria in *N. benthamiana*  
262 leaves [39,40]. In the absence of *P. palmivora* colonization, mCitrine-MpRabG3c and

263 mCitrine-MpRabA1e localized to the tonoplast and to endosomes, respectively (Fig  
264 S9), which is consistent with RabG3c and RabA1e localization in higher plants  
265 [40,41]. During infection, we observed strong labelling of intracellular infection  
266 structures and intracellular hyphae by mCitrine-MpRabG3c (Fig 3B) as well  
267 as mCitrine-MpRabA1e (Fig 3C) at 3 dpi. Together, our results reveal a conserved  
268 host cellular response to invasive haustoria-like intracellular infection structures and  
269 hyphae during the colonization of *Marchantia* cells by *P. palmivora*.

270

271 **A colonization-induced host syntaxin is targeted to intracellular infection  
272 structures.**

273 Plasma membrane-resident syntaxins mediate exocytosis and have been  
274 associated with penetration structures of symbiotic and pathogenic microbes in  
275 several higher plant systems [42,43]. To determine if symbiosis-associated  
276 membrane syntaxins function at intracellular infection structures, we monitored the  
277 expression levels of *Marchantia* SYP13 family homologs during infection and  
278 assessed MpSYP13 localization at pathogen interfaces using mCitrine-tagged  
279 reporter lines [44]. Expression levels of *MpSYP13A* were not affected during  
280 colonization with *P. palmivora*, while *MpSYP13B* displayed significant upregulation  
281 from 2-4 dpi (Fig 4A). In addition, mCitrine-MpSYP13B strongly labelled intracellular  
282 infection structures while maintaining localization at the cell periphery. Conversely,  
283 mCitrine-MpSYP13A localization was unaffected by the presence of intracellular  
284 infection structures (Fig 4B). We observed a number of distinct MpSYP13B  
285 localization patterns, including focal accumulation proximal to hyphal buds of early  
286 developing intracellular infection structures, complete labelling around intracellular  
287 hyphae, and localization to membrane domains of branched intracellular infection  
288 structures (Fig 4C). These results demonstrate that the colonization of *Marchantia* by  
289 *P. palmivora* includes a complex intracellular phase that recruits the MpSYP13B  
290 syntaxin to specific extrainvasive hyphal domains.

291

292 **Co-option of *Marchantia* air chambers for pathogen colonization**

293 The colonization dynamics described thus far have occurred in epidermal  
294 cells and within air chambers of the photosynthetic layer of *M. polymorpha*. In

295 *Marchantia*, loss of function mutations in the E3 ubiquitin ligase NOPPERABO  
296 (NOP1) result in the development of a photosynthetic layer that lacks air chambers  
297 entirely [45]. To determine if air chambers facilitate *P. palmivora* colonization, we  
298 compared the colonization phenotypes of wild-type TAK1 and air chamber-less *nop1*  
299 mutants (Fig 5). As expected, *P. palmivora* ARI-td zoospores inoculated onto TAK1  
300 thalli caused extensive disease symptoms by 7 dpi and continued to 14 dpi when  
301 plants were essentially dead. In comparison, air chamber-less *nop1* mutants  
302 displayed reduced disease symptoms, with plants remaining relatively healthy  
303 throughout the experiment (Fig 5A). To support these observations, we quantified  
304 the expression of pathogen-specific marker genes indicative of biomass (*PpEF1a*)  
305 and sporulation (*PpCdc14*) by qRT-PCR. Compared to wild-type TAK1, pathogen  
306 biomass and sporulation were both significantly reduced in *nop1* mutants (Fig 5B),  
307 which indicates that *P. palmivora* fitness is largely dependent on the presence of air  
308 chambers. This was further supported by microscopic analyses of *P. palmivora*  
309 growth in TAK1 compared to *nop1* plants. Confocal fluorescence microscopy of  
310 sectioned thalli revealed extensive hyphal growth within TAK1 air chambers at 7 dpi,  
311 whereas *nop1* plants displayed only a thin layer of *P. palmivora* hyphae on the dorsal  
312 epidermis (Fig 5C). Moreover, cryo-SEM micrographs confirmed that hyphae travel  
313 from chamber-to-chamber during the colonization of TAK1 thalli, with widespread  
314 hyphal growth observed within air chambers (Fig 5D). In comparison, a network of  
315 surface hyphae was observed on *nop1* thalli and collapsed epidermal cells  
316 containing *P. palmivora* hyphae were occasionally detected late during infection (Fig  
317 5E). In support of this, confocal fluorescence microscopy identified invasive ARI-td  
318 hyphal growth within *nop1* epidermal cells by 3 dpi (Fig 5F). Taken together, our  
319 results demonstrate that *nop1*-dependent changes in thallus architecture impair *P.*  
320 *palmivora* proliferation, suggesting a key role for air chambers in supporting  
321 pathogen colonization.

322

## 323 DISCUSSION

324 In this study, we demonstrate that the broad host-range oomycete *P.*  
325 *palmivora* colonizes the photosynthetic layer of non-vascular liverworts and forms  
326 intracellular hyphal structures resembling a biotrophic interaction. This was  
327 supported by pathogen effector gene expression and by the presence of intracellular

328 hyphal structures that display a biotrophy-associated callose distribution pattern and  
329 associate with host proteins typical of biotrophic interactions. Considered alongside  
330 observations of arbuscules in liverworts and hornworts [7,18,46], the data indicate  
331 that descendants of the earliest diverging land plants have the capacity to  
332 accommodate the biotrophic structures of filamentous eukaryotes within their cells.  
333

334 The colonization of *Marchantia* thalli by *P. palmivora* was largely limited to the  
335 photosynthetic layer, with prolific hyphal growth within and between air chambers.  
336 Colonization assays with the air chamber-less *nop1* mutant revealed that these  
337 structures largely contribute to disease susceptibility in *Marchantia*. This is likely due  
338 to the fact that air chambers offer photosynthetic filament cells rich in carbohydrates  
339 and provide a microenvironment with stable humidity, which is ideal for water molds  
340 such as *Phytophthora*. Our results underscore the need for plants to protect  
341 intercellular spaces important for gas exchange. Such adaptations are present in  
342 higher plants, where analogous intercellular spaces (spongy mesophyll) are  
343 protected by stomata. In many cases, the early detection of pathogens causes  
344 stomatal closure to prevent the colonization of the intercellular space [47]. However,  
345 several pathogens have developed mechanisms to circumvent this strategy, either  
346 by accessing the tissue by other means or by the direct regulation of stomatal guard  
347 cells [48]. Most filamentous pathogens bypass stomata by penetrating host surfaces  
348 using appressoria, a penetration structure that does not appear to play a major role  
349 during the *P. palmivora*-*Marchantia* interaction. Rather, air chambers were accessed  
350 via intra- or intercellular hyphal growth, or through constitutively open pores. *P.*  
351 *palmivora* sporangia often emanated from air pores, similar to observations of  
352 sporangia traversing stomata in angiosperms. The sporophytes of mosses and  
353 hornworts contain stomata, but liverworts do not. How these early forms of stomata  
354 function in response to biotic cues is unknown, however elevated levels of CO<sub>2</sub> do  
355 not alter bryophyte stomata as they do in angiosperms [49]. It is therefore possible  
356 that interactions with pathogenic microbes contributed to the development of stomata  
357 in early land plants. Future comparative studies are required to explore this  
358 relationship between microbial colonization and the development and regulation of  
359 pores involved in gas exchange.  
360

361        The cell walls and surfaces of extant early land plants are less complex than  
362 those of higher plants [50]. How this impacts interactions with pathogenic or  
363 symbiotic microbes remains to be explored. It is tempting to speculate that simple  
364 cell walls are susceptible to invading microbes, however this may not be the case.  
365 For example, previous work in *Marchantia* demonstrated a differential capacity for  
366 powdery mildew spore establishment, such that *Erysiphe trifoliorum* spores  
367 germinated but were destroyed on *M. polymorpha* surfaces while *Oidium*  
368 *neolycopersici* survived and developed appressoria [51]. Whether *O. neolycopersici*  
369 penetrates into *M. polymorpha* cells and establishes infection was not explored by  
370 the authors. A recent study showed that *P. infestans* and *P. capsici* hyphae  
371 penetrate protonemal cells during non-host interactions in moss, whereas  
372 colonization by *P. palmivora* and *P. sojae* was rarely detected [22]. Both *P. infestans*  
373 and *P. capsici* fail to establish biotrophy in moss, as haustoria-like structures were  
374 never observed [22]. In contrast, we demonstrated the colonization of *Marchantia*  
375 thalli by *P. palmivora* rather than *P. infestans*, which was associated with the  
376 development of haustoria-like infection structures. Susceptibility to *P. palmivora* was  
377 greatly enhanced when thalli rather than rhizoids were inoculated with zoospores. In  
378 addition, intercellular hyphal growth within the central storage parenchyma was less  
379 prevalent than growth within air chambers, although plants eventually succumb to  
380 disease and are likely colonized throughout. Based on these observations, we  
381 hypothesize that the central storage region is resistant to pathogen colonization and  
382 requires prolific biotrophic growth within air chambers and a subsequent switch to  
383 necrotrophy for colonization. In contrast, the colonization of liverworts by symbiotic  
384 fungi is abundant within the central storage region but does not extend to the  
385 photosynthetic layer [5]. Collectively, these observations suggest that characteristics  
386 of early land plant tissues and surfaces act as barriers to microbial growth. Future  
387 efforts to identify the structural, genetic, or chemical components responsible for  
388 these phenotypes may reveal interesting similarities and differences to higher plants.  
389

390        We identified several aspects of *P. palmivora* colonization that differ in  
391 *Marchantia* compared to interactions with angiosperms. Appressorial penetration  
392 structures were not prevalent in *Marchantia* as they are in higher plants [27,28]. The  
393 development of oomycete and fungal appressoria require cues such as  
394 hydrophobicity and the perception of cutin monomers characteristic of host cuticles

395 [52,53]. The lack of *P. palmivora* appressoria on *Marchantia* surfaces suggests that  
396 key differences in cuticle composition impact pathogen development on liverwort  
397 surfaces. Indeed, bryophytes are poikilohydric plants that contain simple cuticle-like  
398 layers which afford desiccation tolerance and allows for water absorption through  
399 plant bodies [54]. Interestingly, the fungus *O. neolyopersici* develops appressoria  
400 on *Marchantia* [51], which may suggest differences in the detection of host  
401 surfaces/chemicals compared to *P. palmivora*. The biotrophic phase of the *P.*  
402 *palmivora-Marchantia* interaction was associated with highly branched intracellular  
403 infection structures and intracellular hyphae, whereas interactions in higher plants  
404 are associated with digit-like haustoria and intercellular hyphal growth. Several  
405 genetic markers for biotrophy were expressed during interactions with *Marchantia*,  
406 which suggests the presence of a biotrophic stage despite the under-representation  
407 of typical digit-haustoria. Branched intracellular infection structures were labelled by  
408 host proteins that are typically associated with the extra-haustorial matrix/membrane  
409 [39,40], which suggests a function in biotrophy. Interestingly, a range of intracellular  
410 infection structure morphologies were observed in different liverworts, with *L.*  
411 *cruciata* and *M. paleacea* also demonstrating the presence of digit and knob-like  
412 haustoria, respectively. This suggests that characteristics of liverwort cells influence  
413 the development of intracellular infection structures. Whether this applies to other  
414 bryophyte species remains to be determined, as intracellular infection structures  
415 have not been described in mosses and hornworts.

416

417 The membrane-localized SYP132 syntaxin family is associated with symbiosis  
418 in higher plants. In *Medicago truncatula*, the presence of symbiotic microbes induces  
419 alternative splicing of the SYP132 locus to produce SYP132a, which in turn labels  
420 the infection threads and symbiosomes of nitrogen-fixing rhizobacteria [55,56].  
421 Moreover, silencing of SYP132a suppressed mycorrhizal colonization in *Medicago*  
422 roots, demonstrating the importance of SYP132a in promoting multiple symbiotic  
423 associations [56]. We similarly observed colonization-induced upregulation and  
424 interface localization of a specific membrane syntaxin variant in *Marchantia*  
425 (MpSYP13B), however this was afforded by homologous gene copies rather than  
426 alternative splicing. These data suggest that the evolution of membrane-localized  
427 plant syntaxins was influenced by interactions with symbiotic and pathogenic  
428 microbes, perhaps diverging for roles in general secretory processes or for the

429 accommodation of intracellular microbial structures. We hypothesize that MpSYP13B  
430 represents a specialized syntaxin that evolved to label intracellular structures in  
431 liverworts (this work) similar to SYP132a function in *Medicago* [56].

432

433 Early divergent descendants of the first land plants can accommodate  
434 biotrophic filamentous microbes as diverse as oomycetes (this study) and  
435 mycorrhizal fungi [5]. Our data demonstrate that liverworts encode proteins that  
436 respond and localize to intracellular infection structures and pathogen hyphae, which  
437 suggests that the molecular toolkit required to support intracellular colonisation by  
438 eukaryotic microbes emerged early during land plant evolution. Previous work has  
439 established conserved genetic components required for endosymbiosis, with  
440 experimental evidence demonstrating the presence of functionally conserved  
441 homologs of key symbiosis genes in bryophytes and algae [9,10]. Here we  
442 complement this work by demonstrating the intracellular colonization of liverworts by  
443 a filamentous pathogen that likely hijacks this machinery to cause disease. Together,  
444 these studies suggest an ancient origin for the evolution of microbial accommodation  
445 in plants, which is supported by observations of highly branched microbial structures  
446 and hyphae inside fossilized plant cells [1-4]. In liverworts, we observed highly  
447 branched haustoria-like structures and prolific intracellular hyphal growth that could  
448 appear symbiosis-like in morphology. We therefore suggest caution in attributing the  
449 presence of branched intracellular structures to symbiotic interactions based solely  
450 on the interpretation of fossilized microbial structures or microscopy-based analyses.  
451 Our work further underscores the need to consider pathogenic microbes alongside  
452 symbiotic counterparts when discussing the evolution of microbial accommodation  
453 processes in land plants.

454

## 455 MATERIALS AND METHODS

456

### 457 Plant Growth

458 The plants used in this study are described in Table S2. All plants were cultivated  
459 from gemmae under axenic conditions. *M. polymorpha* and *M. paleacea* were grown  
460 on ½ strength MS (Murashige and Skoog) media (pH 6.7) supplemented with B5

461 vitamins under continuous light ( $70 \mu\text{E m}^{-2} \text{s}^{-1}$ ) at  $22^\circ\text{C}$ . *L. cruciata* were grown in  
462 short-day photoperiod conditions (9 hrs light) at  $20^\circ\text{C}$  on M media [10].

463

#### 464 **Pathogen Growth and Infection Assays**

465 Pathogen strains used in this study are described in Table S3. *P. palmivora* ARI-td  
466 mycelia were maintained by routine passaging on RSA (Rye Sucrose Agar) plates  
467 and zoospores were collected from 7-10 day old cultures on V8 plates as previously  
468 described [27]. *P. infestans* zoospores were collected similar to *P. palmivora*, except  
469 the pathogen was grown solely on RSA plates incubated at  $18^\circ\text{C}$ . Colonization  
470 experiments were performed by applying 10  $\mu\text{L}$  droplets of a zoospore suspension  
471 inoculum ( $10^5$  zoospores  $\text{mL}^{-1}$ ) along the thallus or directly onto rhizoids of 3 week-  
472 old *M. polymorpha* and *M. paleacea* plants. Slower growing *L. cruciata* liverworts  
473 grown from gemmae were infected 6-8 weeks post plating.

474

#### 475 **Microscopy**

476 Epifluorescence microscopy was conducted using a Zeiss Axioimager stereo-  
477 fluorescence microscope with a DsRED filter. All images were processed with  
478 AxioVision software (Rel 4.8). Confocal fluorescence microscopy was performed  
479 using a Leica TCS SP8 equipped with HyD detectors. Settings for pathogen  
480 detection (tdTomato) are described in [27], mCitrine in [44], and aniline blue in [57].  
481 All experiments were performed at least 3 times with similar results. Images were  
482 collected from at least 3 independent plants in at least 2 separate infection sites per  
483 plant. Cross sections of a 200-300  $\mu\text{m}$  thickness were prepared from agarose (3%)  
484 embedded samples using a vibratome. All images were processed using ImageJ.  
485 Cryo-scanning electron microscopy (SEM) was performed essentially as described in  
486 [58], except that ARI-td-infected *M. polymorpha* tissue was used. All samples were  
487 sublimated for 30-60 seconds. Where indicated, samples were analyzed in  
488 backscatter mode to enhance contrast between oomycete and liverwort tissue.

489

#### 490 **Histochemical Staining**

491 Callose staining was performed by gently rinsing whole plants in 0.07 M phosphate  
492 buffer (pH 9), then submerging whole plants in freshly prepared 0.05% aniline blue  
493 (w/v) solution (dissolved in 0.07 M phosphate buffer, pH 9). Plants were incubated in

494 staining solution for 60 minutes and were imaged immediately. A total of six infection  
495 sites (two per plant; three independent plants) were assessed.

496

#### 497 **RNA Isolation, cDNA synthesis, and qRT-PCR analysis**

498 Total RNA was extracted from flash frozen *M. polymorpha* (TAK1) plants that were  
499 mock-inoculated (water) or infected with *P. palmivora* (ARI-td) zoospores at 1, 2, 3,  
500 or 4 days post inoculation (dpi) using the Concert Plant RNA Reagent (Invitrogen,  
501 Cat No. 12322-012) following the manufacturer's instructions. Total RNA was  
502 extracted from axenically cultivated *P. palmivora* ARI-td using the Qiagen Plant  
503 RNeasy kit followed by on-column DNase treatment (for RNAseq) or by using the  
504 Concert Plant RNA Reagent (for qRT-PCR analysis). All samples extracted using the  
505 Concert Plant RNA Reagent were treated with Turbo-DNase reagent (Ambion) to  
506 degrade residual DNA contamination prior to further use. cDNA was synthesized  
507 with SuperScript II reverse transcriptase (Invitrogen) using 2 µg of total RNA  
508 following the manufacturer's instructions. All cDNA samples were diluted 10x with  
509 nuclease free water and stored at - 20 °C until further use. qRT-PCR analyses were  
510 carried out with 2.5 µl of diluted cDNA and LightCycler 480 SYBR Green I master  
511 mix in a 10 µl volume, according to the manufacturer's instructions. Primers for qRT-  
512 PCR analyses were designed using Primer3 [59,60] and are listed in Table S4.  
513 Specificity was validated by analyzing melt curves after each run. Three technical  
514 replicates were analysed for each of the three independent sample replicates for any  
515 given time point/treatment. Calculations of expression levels normalized to internal  
516 controls and statistical analyses were performed using R software. Graphs were  
517 generated in GraphPad Prism6.

518

#### 519 **Cloning and *Marchantia* Transformation**

520 The *Marchantia* *MpRabG3c* and *MpRabA1e* homologs were first identified by BlastP  
521 analysis using homologous sequences from *N. benthamiana*. Full length *MpRabG3c*  
522 (Mapoly0946s0001) and *MpRabA1e* (Mapoly0018s0008) were cloned from cDNA  
523 generated from untreated, 3 week-old *M. polymorpha* (TAK1) plants using Phusion  
524 DNA polymerase (NEB) and gateway compatible primers described in Table S4. Full  
525 length attB sequences were generated using universal attB primers that allow for N-  
526 terminal fusions. Amplicons were recombined into pDONR221 using BP clonase II  
527 (Invitrogen) following manufacturer's instructions. Sequence verified entry clones

528 were then recombined into pMpGWB105 [61] using LR clonase II enzyme mix  
529 (Invitrogen) following manufacturer's instructions. Completed destination constructs  
530 were transformed into *Agrobacterium tumefaciens* GV3101 (pMP90) by  
531 electroporation. *M. polymorpha* transformation was carried out using the  
532 *Agrobacterium*-mediated thallus regeneration method using TAK1 plants [62].  
533 Transformants were selected on solidified ½ MS media (pH 5.6) supplemented with  
534 hygromycin B (15-25 µg mL<sup>-1</sup>) and cefotaxime (125 µg mL<sup>-1</sup>). Stable, non-chimeric  
535 transgenic plants were obtained by propagating gemmae from T1 thalli.  
536

### 537 **Library preparation and sequencing**

538 mRNAs from *M. polymorpha* plants infected with *P. palmivora* at 3 dpi and 4 dpi, and  
539 *P. palmivora* mRNAs from the mycelium sample were purified using Poly(A)  
540 selection from total RNA sample, and then fragmented. cDNA library preparation  
541 was performed with the TruSeq® RNA Sample Preparation Kit (Illumina, US)  
542 according to the manufacturer's protocol. cDNA sequencing of the 9 samples (3 dpi,  
543 4 dpi and mycelium sample, all in triplicates) was performed with Illumina NextSeq  
544 2500 in 100 paired end mode. Samples were de-multiplexed and analyzed further.  
545 The raw fastq data are accessible at <http://www.ncbi.nlm.nih.gov/sra/> with accession  
546 number SRP115544.  
547

### 548 **Expression analysis**

549 Raw reads after quality control with FastQC  
550 (<https://www.bioinformatics.babraham.ac.uk/projects/fastqc/>) were aligned back to  
551 the *P. palmivora* reference genome [63] using STAR (version 2.5.2b) aligner. Raw  
552 counts were obtained with FeatureCounts [64], only uniquely mapped and properly  
553 paired reads were considered further. Differentially expressed genes were identified  
554 with DESeq2 Bioconductor package [65] following pair-wise comparisons between *in*  
555 *planta* and mycelium samples. Differentially expressed genes (absolute LFC ≥ 2 and  
556 adjusted *p*-value ≤ 10<sup>-3</sup>) were used to perform hierarchical clustering of samples.  
557 Heatmaps for the differentially expressed genes were generated using R pheatmap  
558 package [66]. For the final heatmaps rlog-transformed counts median-centered by  
559 gene were used. Scripts used to analyse *P. palmivora* RNA-seq dataset and

560 visualise differentially expressed genes are available in  
561 <https://github.com/gogleva/public-palmivora>.

562

### 563 **Secretome prediction**

564 Putative secreted *P. palmivora* proteins were predicted and manually curated as  
565 described previously [28] based on the gene models from [63].

566

### 567 **ACKNOWLEDGMENTS**

568 For providing materials, we thank Dr. Takashi Ueda (University of Tokyo, Japan), Dr.  
569 Jim Haseloff (University of Cambridge, UK), and Dr. Pierre-Marc Delaux (Paul  
570 Sabatier University, France). For access to *Marchantia polymorpha* genomic  
571 information (<https://phytozome.jgi.doe.gov>), we thank our colleagues at the Joint  
572 Genome Institute (JGI); the work conducted by the U.S. Department of Energy  
573 (DOE) JGI, a DOE Office of Science User Facility, is supported by the Office of  
574 Science of the U.S. DOE under contract DE-AC02-05CH11231. For assistance with  
575 cryo-SEM analysis, we thank Dr. Raymond Wightman (Sainsbury Laboratory,  
576 University of Cambridge). We thank Dr. Sophien Kamoun (The Sainsbury  
577 Laboratory, Norwich) for critically assessing an early draft of this manuscript. For  
578 additional critical and technical support, we thank Dr. Edouard Evangelisti, Dr. Ruth  
579 Le Fevre, Dr. Temur Yunusov, Lara Busby, and all members of the Schornack  
580 group.

581

### 582 **FUNDING**

583 This research was funded by the Gatsby Charitable Foundation (RG62472),  
584 the Royal Society (RG69135), the BBSRC OpenPlant initiative (BB/L014130/1) and  
585 the Natural Environment Research Council (NERC; NE/N00941X/1).

586

### 587 **REFERENCES**

588

589 [1] Remy W, Taylor TN, Hass H, Kerp H. Four hundred-million-year-old vesicular  
590 arbuscular mycorrhizae. Proc. Natl. Acad. Sci. USA 1994; 91(25): 11841-11843.

591

- 592 [2] Taylor TN, Remy W, Hass H, Kerp H. Fossil arbuscular mycorrhizae from the  
593 early devonian. *Mycologia* 1995; 87(4): 560-73.  
594
- 595 [3] Krings M, Taylor TN, Hass H, Kerp H, Dotzler N, Hermsen EJ. Fungal  
596 endophytes in a 400-million-yr-old land plant: infection pathways, spatial distribution,  
597 and host responses. *New Phytologist* 2007; 174(3): 648-57.  
598
- 599 [4] Strullu-Derrien C, Kenrick P, Pressel S, Duckett JG, Rioult J-P, Strullu D-G.  
600 Fungal associations in Horneophyton ligneri from the Rhynie Chert (c. 407 million  
601 year old) closely resemble those in extant lower land plants: novel insights into  
602 ancestral plant-fungus symbioses. *New Phytologist* 2014; 203(3): 964-79.  
603
- 604 [5] Ligrone R, Carafa A, Lumini E, Bianciotto V, Bonfante P, Duckett JG.  
605 Glomeromycotan associations in liverworts: a molecular, cellular, and taxonomic  
606 analysis. *American Journal of Botany* 2007; 94(11): 1756-77.  
607
- 608 [6] Adams DG, Duggan PS. Cyanobacteria-bryophyte symbioses. *Journal of  
609 Experimental Botany* 2008; 59(5): 1047-58.  
610
- 611 [7] Pressel S, Bidartondo MI, Ligrone R, Duckett JG. Fungal symbioses in  
612 bryophytes: new insights in the twenty first century. *Phytotaxa* 2010; 9(30): 238-53.  
613 doi: <http://dx.doi.org/10.11646/phytotaxa.9.1.13>  
614
- 615 [8] Desiro A, Duckett JG, Pressel S, Villarreal JC, Bidartondo MI. Fungal symbioses  
616 in hornworts: a chequered history. *Proc Biol Sci* 2013; 280(1759): 20130207. doi:  
617 <http://dx.doi.org/10.1098/rspb.2013.0207>  
618
- 619 [9] Wang B, Yeun LH, Xue J-Y, Liu Y, Ane J-M, Qiu Y-L. Presence of three  
620 mycorrhizal genes in the common ancestor of land plants suggests a key role of  
621 mycorrhizas in the colonization of land by plants. *New Phytologist* 2010; 186(2): 514-  
622 25.  
623
- 624 [10] Delaux P-M, Radhakrishnan GV, Jayaraman D, Cheema J, Malbreil M,  
625 Volkening JD, Sekimoto H, Nishiyama T, Melkonian M, Pokorny L, Rothfels CJ,

- 626 Sederoff HW, Stevenson DW, Surek B, Zhang Y, Sussman MR, Dunand C, Morris  
627 RJ, Roux C, Wong G, Oldroyd G, Ane J-M. Algal ancestor of land plants was  
628 preadapted for symbiosis. *Proc. Natl. Acad. Sci. USA* 2015; 112(43): 13390-13395.  
629
- 630 [11] Petre B, Kamoun S. How do filamentous pathogens deliver effector proteins into  
631 plant cells? *PLoS Biology* 2014; 12(2):e1001801. doi: 10.1371/journal.pbio.1001801.  
632
- 633 [12] Roth R, Paszkowski U. Plant carbon nourishment of arbuscular mycorrhizal  
634 fungi. *Current Opinion in Plant Biology* 2017; 39: 50-56  
635
- 636 [13] Parniske M. Intracellular accommodation of microbes by plants: a common  
637 developmental program for symbiosis and disease? *Current Opinion in Plant Biology*  
638 2000; 3(4): 320-28.  
639
- 640 [14] Rey T, Schornack S. Interactions of beneficial and detrimental root-colonizing  
641 filamentous microbes with plant hosts. *Genome Biology* 2013; 14(6): 121. doi:  
642 10.1186/gb-2013-14-6-121.  
643
- 644 [15] Ivanov S, Fedorova E, Bisseling T. Intracellular plant microbe associations:  
645 secretory pathways and the formation of perimicrobial compartments. *Current  
646 Opinion in Plant Biology* 2010; 13(4): 372-77  
647
- 648 [16] Zeilinger S, Gupta VK, Dahms TES, Silva RN, Singh HB, Upadhyay RS, Gomes  
649 EV, Tsui CKM, Nayak SC. Friends or foes? Emerging insights from fungal  
650 interactions with plants. *FEMS Microbiology Reviews* 2016; 40(2): 182-207  
651
- 652 [17] Qiu YL, Li L, Wang B, Chen Z, Knoop V, Groth-Molanek M, Dombrovska O, Lee  
653 J, Kent L, Rest L, Estabrook GF, Hendry TA, Taylor DW, Testa CM, Ambros M,  
654 Crandall-Stotler B, Duff RJ, Stech M, Frey W, Quandt D, Davis CC. The deepest  
655 divergences in land plants inferred from phylogenomic evidence. *Proceedings of the  
656 National Academy of Sciences USA* 2006; 103(42): 15511-6  
657

- 658 [18] Renzaglia KS, Schuette S, Duff RJ, Ligrone R, Shaw AJ, Mishler BD, Duckett  
659 JG. Bryophyte phylogeny: advancing the molecular and morphological frontiers. *The*  
660 *Bryologist* 2007; 110(2): 179-213.  
661  
662 [19] Cox CJ, Li B, Foster PG, Embley TM, Civan P. Conflicting phylogenies for early  
663 land plants are caused by composition biases among synonymous substitutions.  
664 *Systematic Biology* 2014; 63(2): 272-79  
665  
666 [20] Ruhfel BR, Gitzendanner MA, Soltis PS, Soltis DE, Burleigh JG. From algae to  
667 angiosperms-inferring the phylogeny of green plants (Viridiplantae) from 360 plastid  
668 genomes. *BMC Evolutionary Biology* 2014; 14: 23. doi: 10.1186/1471-2148-14-23.  
669  
670 [21] Ponce de Leon I. The moss *Physcomitrella patens* as a model system to study  
671 interactions between plants and phytopathogenic fungi and oomycetes. *J. Pathogens*  
672 2011; 2011:719873. doi: 10.4061/2011/719873  
673  
674 [22] Overdijk EJ, De Keijzer J, De Groot D, Schoina C, Bouwmeester K, Ketelaar T,  
675 Govers F. Interaction between the moss *Physcomitrella patens* and Phytophthora: a  
676 novel pathosystem for live-cell imaging of subcellular defence. *J. Microscopy* 2016;  
677 263(2): 171-80  
678  
679 [23] Ponce de Leon I, Montesano M. Adaptation mechanisms in the evolution of  
680 moss defenses to microbes. *Frontiers in Plant Science* 2017; 8: 366. doi:  
681 10.3389/fpls.2017.00366  
682  
683 [24] Ishizaki K, Nishihama R, Yamato KT, Kohchi T. Molecular genetic tools and  
684 techniques for *Marchantia polymorpha* research. *Plant and Cell Physiology* 2016;  
685 57(2): 262-70  
686  
687 [25] Shimamura M. *Marchantia polymorpha*: taxonomy, phylogeny, and morphology  
688 of a model system. *Plant and Cell Physiology* 2016; 57(2): 230-56.  
689

- 690 [26] Rey T, Chatterjee A, Buttay M, Toulotte J, Schornack S. *Medicago truncatula*  
691 symbiosis mutants affected in the interaction with a biotrophic root pathogen. *New*  
692 *Phytologist* 2015; 206(2): 385-95.
- 693
- 694 [27] Le Fevre R, O'Boyle B, Moscou MJ, Schornack S. (2016) Colonization of barley  
695 by the broad-host hemibiotrophic pathogen *Phytophthora palmivora* uncovers a leaf  
696 development-dependent involvement of Mlo. *Molecular Plant Microbe Interactions*  
697 2016; 29(5): 385-95.
- 698
- 699 [28] Evangelisti E, Goleva A, Hainaux T, Doumane M, Tulin F, Quan C, Yunusov T,  
700 Floch K, Schornack S. Time-resolved dual root-microbe transcriptomics reveals early  
701 induced *Nicotiana benthamiana* genes and conserved infection-promoting  
702 *Phytophthora palmivora* effectors. *BMC Biology* 2017; 15(1): 39. doi:  
703 10.1186/s12915-017-0379-1
- 704
- 705 [29] Judelson HS, Blanco FA. The spores of *Phytophthora*: weapons of the plant  
706 destroyer. *Nat. Rev. Microbiol.* 2005; 3(1): 47-58.
- 707
- 708 [30] Morgan W, Kamoun S. RXLR effectors of plant pathogenic oomycetes. *Current*  
709 *Opinion in Microbiology* 2007; 10(4): 332-38.
- 710
- 711 [31] Anderson RG, Deb D, Fedkenheuer K, McDowell JM. Recent progress in RXLR  
712 effector research. *Molecular Plant-Microbe Interactions* 2015; 28(10): 1063-72.
- 713
- 714 [32] Wang S, Boevink PC, Welsh L, Zhang R, Whisson SC, Birch PRJ. Delivery of  
715 cytoplasmic and apoplastic effectors from *Phytophthora infestans* haustoria by  
716 distinct secretion pathways. *New Phytologist* 2017; 216(1): 205-215
- 717
- 718 [33] Hardham AR. Cell biology of plant-oomycete interactions. *Cellular Microbiology*  
719 2007; 9(1): 31-9
- 720
- 721 [34] Torres GA, Sarria GA, Martinez G, Varon F, Drenth A, Guest D. Bud rot caused  
722 by *Phytophthora palmivora*: a destructive emerging disease of oil palm.  
723 *Phytopathology* 2016; 106(4): 320-9.

- 724
- 725 [35] Avrova AO, Boevink PC, Young V, Grenville-Briggs LJ, van West P, Birch PR,  
726 Whisson SC. A novel *Phytophthora infestans* haustorium-specific membrane protein  
727 is required for infection of potato. *Cellular Microbiology* 2008; 10(11): 2271-84
- 728
- 729 [36] Ah Fong AMV, Judelson HS. Cell cycle regulator Cdc14 is expressed during  
730 sporulation but not hyphal growth in the fungus-like oomycete *Phytophthora*  
731 *infestans*. *Molecular Microbiology* 2003; 50(2): 487-94.
- 732
- 733 [37] Bellincampi D, Cervone F, Lionetti V. Plant cell wall dynamics and wall-related  
734 susceptibility in plant-pathogen interactions. *Frontiers in Plant Science* 2014; 5: 228  
735 doi: 10.3389/fpls.2014.00226
- 736
- 737 [38] Faulkner C. A cellular backline: specialization of host membranes defence.  
738 *Journal of Experimental Botany* 2015; 66(6): 1565-71.
- 739
- 740 [39] Bozkurt TO, Belhaj K, Dagdas YF, Chaparro-Garcia A, Wu CH, Cano LM,  
741 Kamoun S. Rerouting of plant late endocytic trafficking toward a pathogen interface.  
742 *Traffic* 2015; 16(2): 204-26.
- 743
- 744 [40] Lu YJ, Schornack S, Spallek T, Geldner N, Chory J, Schellmann S, Schumacher  
745 K, Kamoun S, Robatzek S. Patterns of plant subcellular responses to successful  
746 oomycete infections reveal differences in host cell reprogramming and endocytic  
747 trafficking. *Cell Microbiology* 2012; 14(5): 682-97.
- 748
- 749 [41] Zhang C, Hicks GR, Raikhel NV. Plant vacuole morphology and vacuolar  
750 trafficking. *Frontiers in Plant Science* 2014; 5: 476. doi: 10.3389/fpls.2014.00476
- 751
- 752 [42] Gu Y, Zavaliev R, Dong X. Membrane trafficking in plant immunity. *Molecular  
753 Plant* 2017; 10(8): 1026-1034
- 754
- 755 [43] Kanazawa T, Ueda T. Exocytic trafficking pathways in plants: why and how they  
756 are redirected. *New Phytologist* 2017; 215(3): 952-57
- 757

- 758 [44] Kanazawa T, Era A, Minamino N, Shikano Y, Fujimoto M, Uemura T, Nishihama  
759 R, Yamato KT, Ishizaki K, Nishiyama T, Kohchi T, Nakano A, Ueda T. SNARE  
760 molecules in *Marchantia polymorpha*: unique and conserved features of the  
761 membrane fusion machinery. *Plant and Cell Physiology* 2016; 57(2): 307-24.  
762
- 763 [45] Ishizaki K, Mizutani M, Shimamura M, Nishihama R, Kohchi T. Essential role of  
764 the E3 ubiquitin ligase nopperabo1 in schizogenous intercellular space formation in  
765 the liverwort *Marchantia polymorpha*. *Plant Cell* 2013; 25(10): 4075-84  
766
- 767 [46] Schussler A. Glomus claroideum forms an arbuscular mycorrhiza-like symbiosis  
768 with the hornwort *Anthoceros punctatus*. *Mycorrhiza* 2000; 10(1): 15-21  
769
- 770 [47] McLachlan DH, Kopischke M, Robatzek S. Gate control: guard cell regulation by  
771 microbial stress. *New Phytologist* 2014; 203(4): 1049-63.  
772
- 773 [48] Melotto M, Zhang L, Oblessuc PR, He S-Y. Stomatal defense a decade later.  
774 *Plant Physiology* 2017; 174(2): 561-71.  
775
- 776 [49] Field KJ, Duckett JG, Cameron DD, Pressel S. Stomatal density and aperture in  
777 non-vascular land plants are non-responsive to above-ambient atmospheric CO<sub>2</sub>  
778 concentrations. *Annals of Botany* 2015; 115(6): 915-22  
779
- 780 [50] Sarkar P, Bosneaga E, Auer M. Plant cell walls throughout evolution: towards a  
781 molecular understanding of their design principles. *Journal of Experimental Botany*  
782 2009; 60(13): 3615-35  
783
- 784 [51] Takikawa Y, Senga Y, Nonomura T, Matsuda Y, Kakutani K, Toyoda H.  
785 Targeted destruction of fungal structures of *Erysiphe trifoliorum* on flat leaf surfaces  
786 of *Marchantia polymorpha*. *Plant Biology* 2014; 16(1): 291-5.  
787
- 788 [52] Latijnhouwers M, de Wit PJGM, Govers F. Oomycetes and fungi: similar  
789 weaponry to attack plants. *Trends in Microbiology* 2003; 11(10): 462-69.  
790

- 791 [53] Wang E, Schornack S, Marsh JF, Gobbato E, Schwessinger B, Eastmond P,  
792 Schultze M, Kamoun S, Oldroyd GED. A common signaling process that promotes  
793 mycorrhizal and oomycete colonization of plants. *Current Biology* 2012; 22(23):  
794 2242-46.
- 795
- 796 [54] Ligrone R, Duckett JG, Renzaglia KS. Major transitions in the evolution of early  
797 land plants: a bryological perspective. *Annals of Botany* 2012; 109(5): 851-71
- 798
- 799 [55] Catalano CM, Czymbek KJ, Gann JG, Sherrier DJ. *Medicago truncatula*  
800 syntaxin SYP132 defines the symbosome membrane and infection droplet  
801 membrane in root nodules. *Planta* 2007; 225(3): 541-50
- 802
- 803 [56] Pan H, Oztas O, Zhang X, Wu X, Stonoha C, Wang E, Wang B, Wang D. A  
804 symbiotic SNARE protein generated by alternative termination of transcription.  
805 *Nature Plants* 2016; 2: 15197. doi: 10.1038/nplants.2015.197
- 806
- 807 [57] Caillaud M-C, Wirthmueller L, Sklenar J, Findlay K, Piquerez SJM, Jones AME,  
808 Robatzek S, Jones JDG, Faulkner C. The plasmodesmatal protein PDLP1 localises  
809 to haustoria-associated membranes during downy mildew infection and regulates  
810 callose deposition. *PLOS Pathogens* 2014; 10(10): e1004496. doi:  
811 <https://doi.org/10.1371/journal.ppat.1004496>
- 812
- 813 [58] Wightman R, Wallis S, Aston P. Hydathode pit development in the alpine plant  
814 *Saxifraga cochlearis*. *Flora* 2017; 233: 99-108. doi:  
815 <https://doi.org/10.1016/j.flora.2017.05.018>
- 816
- 817 [59] Koressaar T, Remm M. Enhancements and modifications of primer design  
818 program Primer3. *Bioinformatics* 2007; 23(10): 1289-91
- 819
- 820 [60] Untergasser A, Cutcutache I, Koressaar T, Ye J, Faircloth BC, Remm M, Rozen  
821 SG. Primer3 – new capabilities and interfaces. *Nucleic Acids Research* 2012; 40(15):  
822 e115. doi: 10.1093/nar/gks596
- 823

824 [61] Ishizaki K, Nishihama R, Ueda M, Inoue K, Ishida S, Nishimura Y, Shikanai T,  
825 Kohchi T. Development of gateway binary vector series with four different selection  
826 markers for the liverwort *Marchantia polymorpha*. PLoS ONE 2015; 10(9): e0138876.  
827 doi: <https://doi.org/10.1371/journal.pone.0138876>

828

829 [62] Kubota A, Ishizaki K, Hosaka M, Kohchi T. Efficient agrobacterium-mediated  
830 transformation of the liverwort *Marchantia polymorpha* using regenerating thalli.  
831 Biosci. Biotechnol. Biochem. 2013; 77(1): 167-77

832

833 [63] Ali SS, Shao J, Lary DJ, Kronmiller BA, Shen D, Strem MD, Amoako-Attah I,  
834 Akrofi AY, Begoude BAD, ten Hoopen GM, Coulibaly K, Kebe BI, Melnick RL,  
835 Guiltinan MJ, Tyler BM, Meinhardt LW, Bailey BA. Phytophthora megakarya and  
836 Phytophthora palmivora, closely related causal agents of cacao black pod rot,  
837 underwent increases in genome sizes and gene numbers by different mechanisms.  
838 Genome Biology and Evolution 2017; 9(3): 536-57

839

840 [64] Liao Y, Smyth GK, Shi W. featureCounts: an efficient general purpose program  
841 for assigning sequence reads to genomic features. Bioinformatics 2014; 30(7): 923-  
842 30

843

844 [65] Love MI, Huber W, Anders S. Moderated estimation of fold change and  
845 dispersion for RNA-seq data with DESeq2. Genome Biology 2014; 15(12): 550  
846 <https://doi.org/10.1186/s13059-014-0550-8>

847

848 [66] Kolde R. pheatmap: Pretty Heatmaps. R package version 1.0.8. 2015

849

## 850 SUPPORTING INFORMATION

### 851 Fig S1. Rhizoid inoculations do not reliably lead to colonization

852 (A) Disease symptoms at 7 days post inoculation (dpi) of 3-week-old *M. polymorpha*  
853 (TAK1) plants that were inoculated with *P. palmivora* ARI-td zoospores or water  
854 directly onto rhizoids.

855 **(B)** Confocal fluorescence microscopy demonstrating *P. palmivora* ARI-td growth on  
856 3-week-old *M. polymorpha* rhizoids from 1-3 dpi. Micrographs represent z-stack  
857 projections of merged bright field and tdTomato channels. Scale bars = 50 µm.

858 **Fig S2. *P. palmivora* colonizes TAK1 thalli.** Confocal fluorescence microscopy  
859 demonstrating *P. palmivora* ARI-td growth on 3-week-old *M. polymorpha* thalli from  
860 1-4 days post inoculation (dpi). Micrographs represent z-stack projections. The  
861 merged micrographs display red pathogen fluorescence (tdTomato) overlaid on top  
862 of chlorophyll autofluorescence (turquoise). Scale bars = 100 µm.

863 **Fig S3. *P. palmivora* hyphae access the storage region during necrotrophy.**  
864 Confocal fluorescence microscopy demonstrating the co-occurrence of *P. palmivora*  
865 ARI-td hyphae and necrotrophic disease symptoms in the storage region of *M.*  
866 *polymorpha* thalli at 7 days post inoculation (dpi). Red pathogen fluorescence is  
867 merged with bright field images. Micrographs represent z-stacked images. Scale  
868 bars = 100 µm.

869 **Fig S4. Biotrophic colonization of the photosynthetic layer in *Marchantia***  
870 ***paleacea* and *Lunularia cruciata*.**

871 **(A)** Confocal fluorescence microscopy of sectioned thalli of *M. paleacea* and *L.*  
872 *cruciata* colonized by *P. palmivora* ARI-td at 7 days post inoculation (dpi). Z-stacked  
873 images represent red pathogen fluorescence (tdTomato) merged with the bright field  
874 channel. Colonized air chambers are denoted by arrows. Scale bars = 100 µm

875 **(B)** Confocal fluorescence microscopy demonstrating haustoria morphology in *P.*  
876 *palmivora* ARI-td-colonized *M. paleacea* (*Mpa*) and *L. cruciata* (*Lc*) thalli at 3 dpi. Z-  
877 stacked images display red pathogen fluorescence (ARI-td) merged with plastid  
878 autofluorescence. Scale bars = 10 µm.

879 **Fig S5. *P. palmivora* strains vary in aggressiveness in TAK1.**

880 Disease symptoms of *M. polymorpha* TAK1 plants inoculated with water (mock) or  
881 zoospores of *P. palmivora* strains 7 days post inoculation (dpi). Images displayed are  
882 representative of consistent symptoms observed from 8-16 infected plants per strain.

883 **Fig S6. *P. infestans* does not cause disease symptoms on TAK1**

884 Disease progression of *M. polymorpha* TAK1 plants inoculated with water, *P.*  
885 *palmivora* (ARI-td) zoospores or *P. infestans* (*Pi*88069-td) zoospores. Images display  
886 consistent disease symptoms (n=8) at 1, 3, 5, and 7 days post inoculation (dpi).

887 **Fig S7. Validation of colonization-induced *P. palmivora* genes**

888 qRT-PCR analysis of *P. palmivora* (ARI-td) genes identified by RNA-seq analyses.  
889 Expression levels were quantified in an axenically propagated MZ (mycelia +  
890 zoospores) sample and during the colonization of *M. polymorpha* thalli from 1-4 days  
891 post inoculation (dpi). Expression levels were quantified relative to internal controls  
892 *PpEF1a* and *PpWS21*. Different letters indicate statistically significant differences in  
893 expression levels (ANOVA, Tukey' HSD, p < 0.05). Performed twice with similar  
894 results.

895 **Fig S8. Callose does not envelope *P. palmivora* infection structures**

896 Confocal fluorescence microscopy of aniline blue stained *M. polymorpha* TAK1 thalli  
897 infected with *P. palmivora* ARI-td at 3 days post inoculation (dpi). Images represent  
898 z-stack projections displaying red fluorescence from the pathogen (tdTomato),  
899 callose deposition through aniline blue staining (white), bright field, or tdTomato  
900 merged with aniline blue. Asterisks (\*) denote intracellular infection structures that  
901 are not enveloped by callose.

902 **Fig S9. Subcellular localization of MpRabA1e and MpRabG3c**

903 **(A)** Confocal fluorescence microscopy showing subcellular localization patterns of  
904 MpRabA1e in 35S:mCitrine-MpRabA1e/TAK1 gemmae. Micrographs display  
905 mCitrine fluorescence, plastid autofluorescence (magenta), both channels merged,  
906 or bright field images. Scale bars = 10 µm.

907 **(B)** Confocal fluorescence microscopy showing subcellular localization patterns of  
908 MpRabG3c in 35S:mCitrine-MpRabG3c/TAK1 gemmae. Micrographs display  
909 mCitrine fluorescence, plastid autofluorescence (magenta), both channels merged,  
910 or bright field images. Scale bars = 10 µm.

911 **S1 Table. Colonization-induced *P. palmivora* genes (abs(LFC) >= 2, p-value≤10<sup>-3</sup>)**

913 **S2 Table. Plants used in this study.**

914 **S3 Table. Pathogen strains used in this study**

915    **S4 Table. Primers used in this study.**

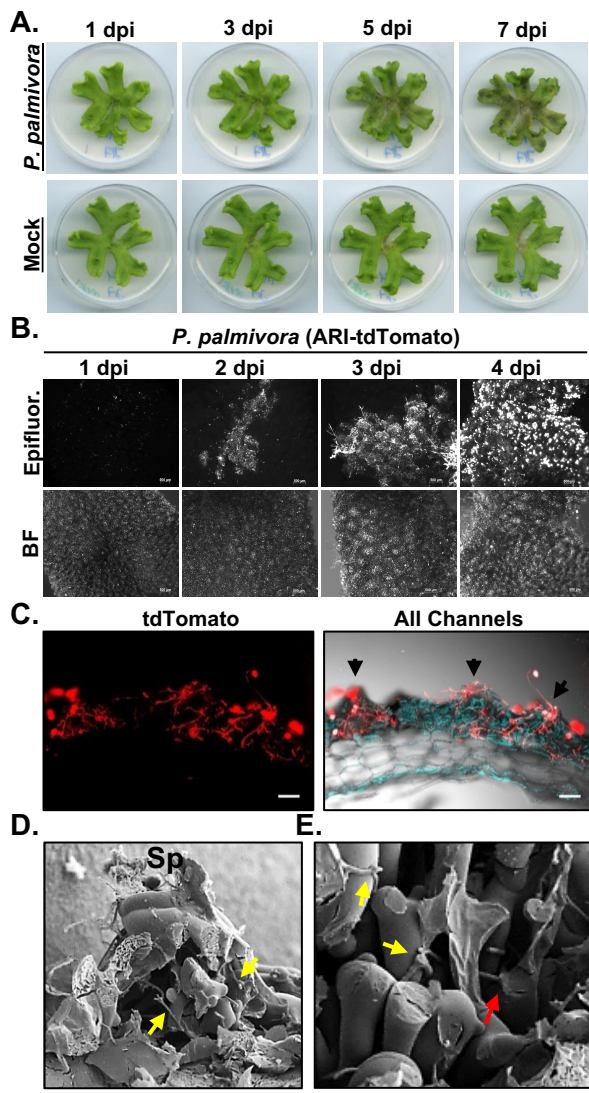


**Fig 1. *Phytophthora palmivora* colonizes the photosynthetic layer of *Marchantia polymorpha*.**

**(A)** Disease symptoms of 3-week-old *M. polymorpha* TAK1 (male) thalli inoculated with *P. palmivora* ARI-td zoospores or water (mock) over a 7-day time course (dpi – days post inoculation). **(B)** Epifluorescence microscopy demonstrating the spread of *P. palmivora* growth across TAK1 thalli from 1-4 dpi. Epifluorescence (Epifluor.) from the pathogen is displayed alongside bright field (BF) images. Scale bars = 500 µm. **(C)** Confocal fluorescence microscopy of sectioned TAK1 thalli infected with *P. palmivora* at 7 dpi. Z-stack projections of red fluorescence from the pathogen is displayed alone (tdTomato) or merged with all channels (bright-field and plastid auto-fluorescence in turquoise). Arrows indicate air pores. Scale bars = 100 µm. **(D-E)** CryoSEM (scanning electron microscopy) of TAK1 thalli colonized by *P. palmivora* at 7 dpi. (D) Mechanically fractured air chamber demonstrating hyphal growth within the chamber (yellow arrows) and sporangia (Sp) at the air pore. (E) Intercellular (yellow arrows) and intracellular (red arrow) associations between *P. palmivora* hyphae and photosynthetic filaments within *M. polymorpha* air chambers. Scale bars = 20 µm. Experiments (A-E) were performed at least three times with similar results.

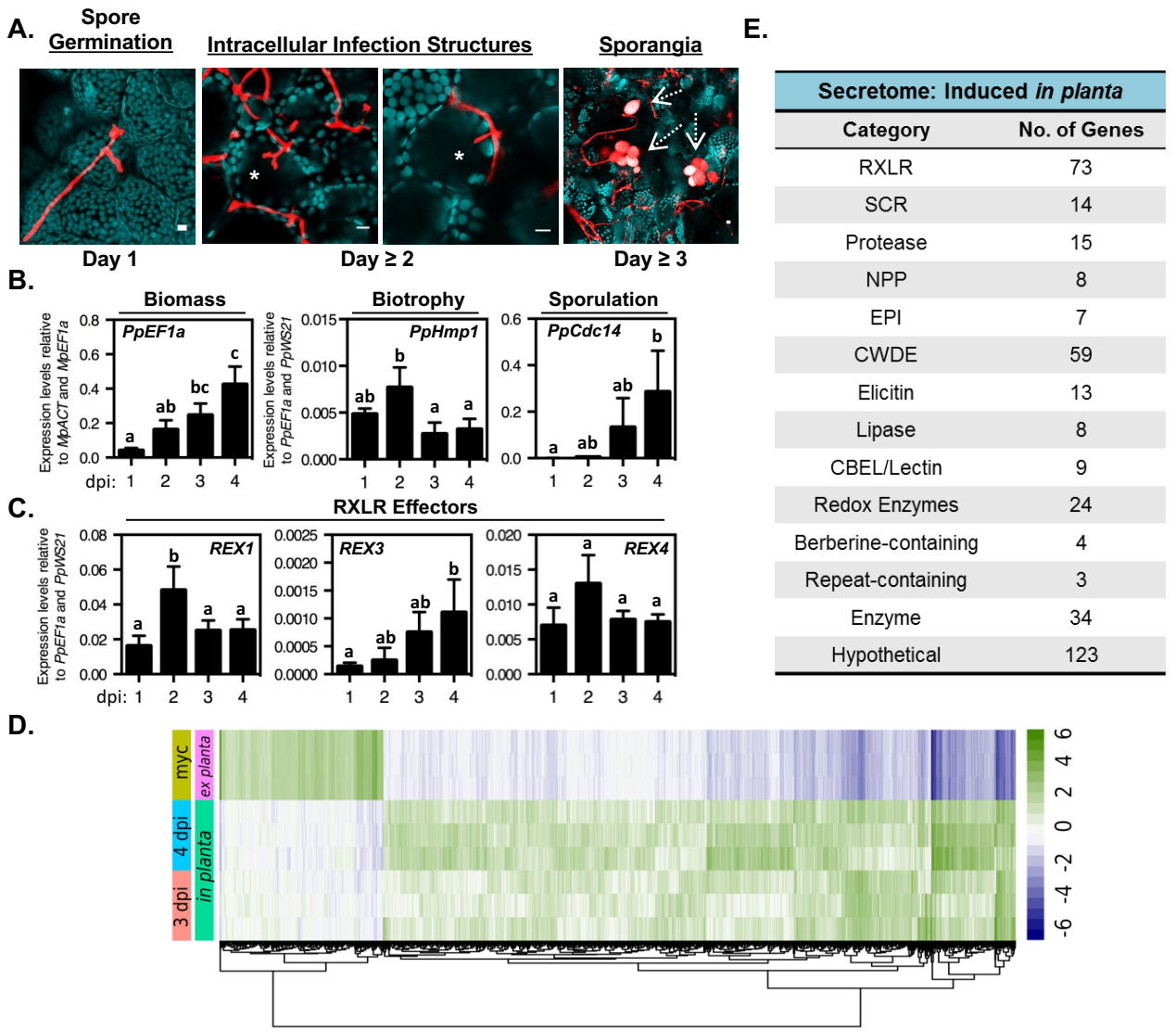


**Fig 2. *Phytophthora palmivora* establishes a biotrophic interaction and completes a full infection cycle in *Marchantia*.**

**(A)** Confocal fluorescence microscopy demonstrating key morphological transitions in *P. palmivora* lifestyle during the colonization of TAK1 plants from 1-3 days post inoculation (dpi). Z-stack projections of pathogen fluorescence merged with plastid auto-fluorescence (turquoise). Intracellular infection structures are denoted by an asterisk (\*). Sporangia are indicated by dashed arrows. Scale bars = 10 µm. **(B)** Quantification of *P. palmivora* lifestyle marker genes during the colonization of TAK1 thalli from 1-4 dpi via qRT-PCR analysis. Pathogen biomass (*PpEF1a*) was quantified relative to *M. polymorpha* biomass markers (*MpACT* and *MpEF1a*). Biotrophy (*PpHmp1*) and sporulation (*PpCdc14*) marker genes were quantified relative to pathogen biomass controls (*PpEF1a* and *PpWS21*). Different letters signify statistically significant differences in transcript abundance (ANOVA, Tukey's HSD p < 0.05). **(C)** Quantification of *P. palmivora* RXLR effector gene transcripts during the colonization of TAK1 thalli from 1-4 dpi via qRT-PCR analysis. RXLR effector (*REX1*, *REX3*, *REX4*) gene expression was quantified relative to *P. palmivora* biomass (*PpEF1a* and *PpWS21*). Different letters signify statistically significant differences in transcript abundance (ANOVA, Tukey's HSD p < 0.05). **(D)** *P. palmivora* transcriptome. Hierarchical clustering of differentially expressed genes between *in planta* (3 and 4 dpi) and axenically grown mycelium transcriptomes ( $\text{LFC} \geq 2$ ,  $p\text{-value} \leq 10^{-3}$ ). Rlog-transformed counts, median-centered by gene are shown. **(E)** *P. palmivora* secretome. Summary of functional categories of 394 genes encoding putative secreted proteins up-regulated during *P. palmivora* infection of *M. polymorpha*. Experiments (A-C) were performed at least three times with similar results.

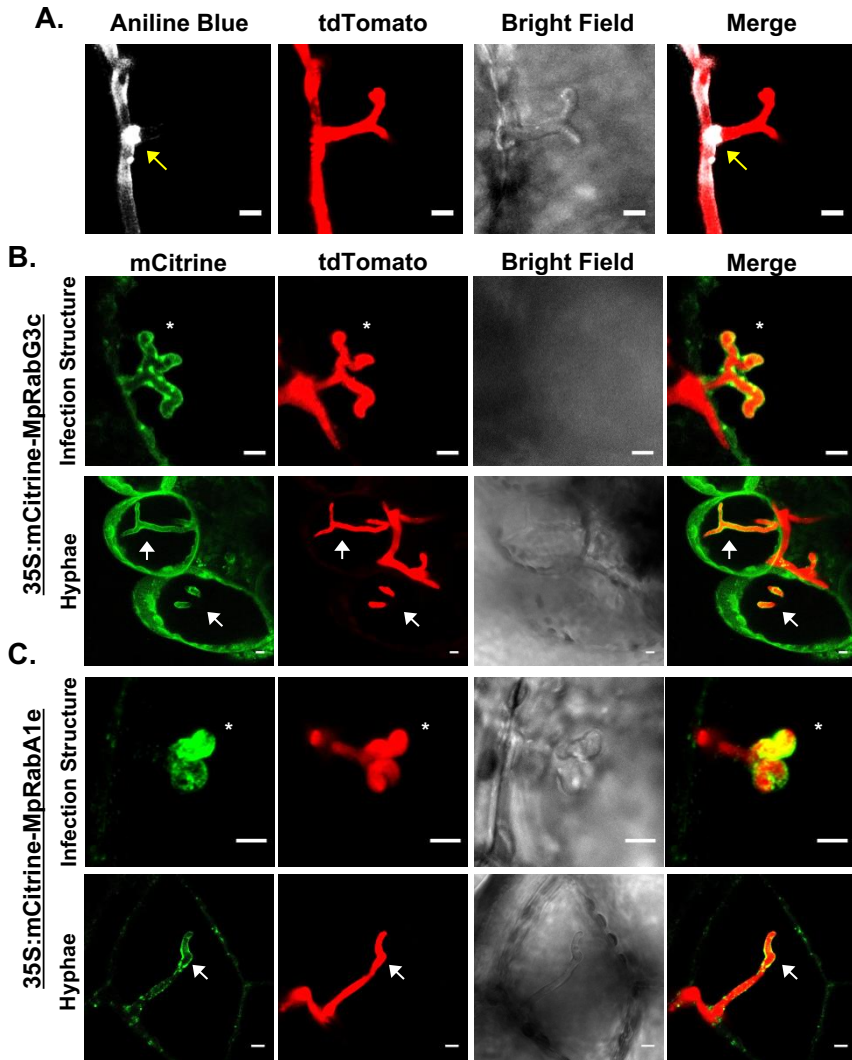


**Fig 3. Host Cellular Responses to Invading Oomycete Structures**

(A) Detection of callose deposition at *P. palmivora* ARI-td intracellular infection structures at 3 days post inoculation (dpi). Arrows indicate callose deposition at the peripheral neck region of the invading intracellular infection structure (denoted by an asterisk \*). Scale bar = 5  $\mu$ m. (B) MpRabG3c co-localization with invading *P. palmivora* ARI-td structures in 35S:mCitrine-MpRabG3c plants at 3 dpi. Infection structures are indicated with asterisks (\*) while intracellular hyphae are denoted by arrows. Z-stack projections are displayed. Scale bars = 5  $\mu$ m. (C) MpRabA1e co-localization with invading *P. palmivora* ARI-td structures in 35S:mCitrine-MpRabA1e plants at 3 dpi. Z-stack projections are displayed. Scale bars = 5  $\mu$ m. Experiments (A-C) were performed three times with similar results.

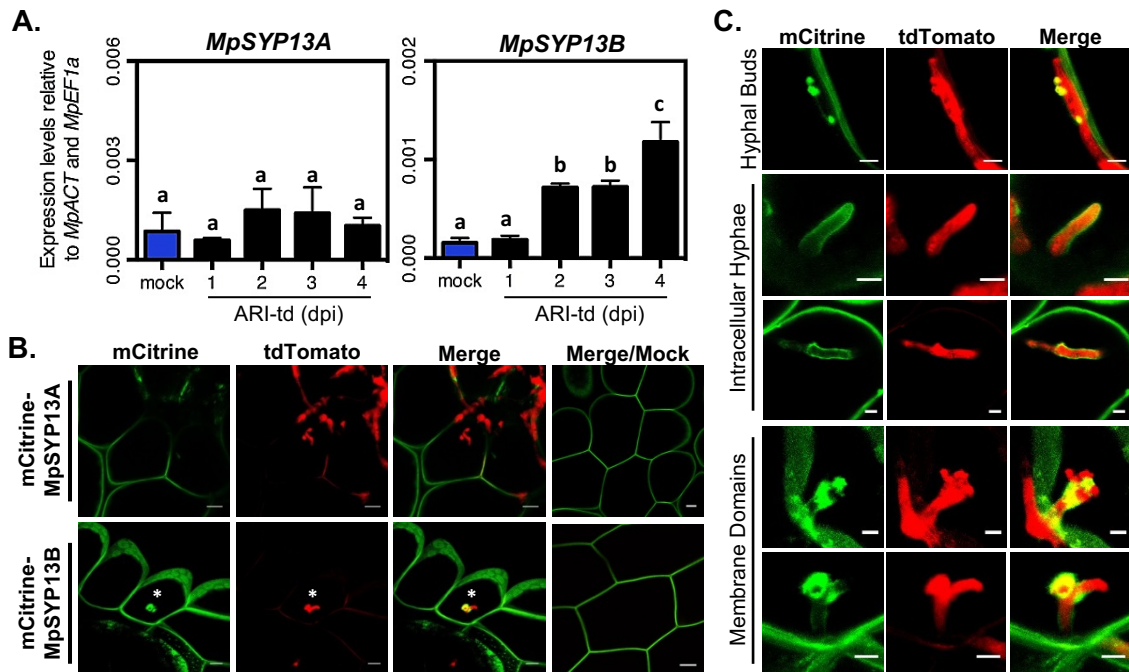


**Fig 4. A colonization-induced host syntaxin accumulates at intracellular infection structures.**

**(A)** qRT-PCR analysis of *MpSYP13A* and *MpSYP13B* transcripts in mock-treated or *P. palmivora*-colonized (ARI-td) TAK1 plants from 1-4 days post inoculation (dpi). Expression values are shown relative to internal *MpACT* and *MpEF1a* controls. Different letters signify statistically significant differences in transcript abundance (ANOVA, Tukey's HSD p < 0.05).

**(B)** Confocal fluorescence microscopy demonstrating mCitrine-MpSYP13A/B localization in cells containing *P. palmivora* (ARI-td) intracellular infection structures at 3 dpi. Asterisks denote intracellular infection structures. Scale bars = 10 µm.

**(C)** Patterns of mCitrine-MpSYP13B localization in *P. palmivora*-colonized (ARI-td) plants, including a close-up image of the structure displayed in (B). Scale bars = 5 µm. Experiments (A-C) were performed three times with similar results.

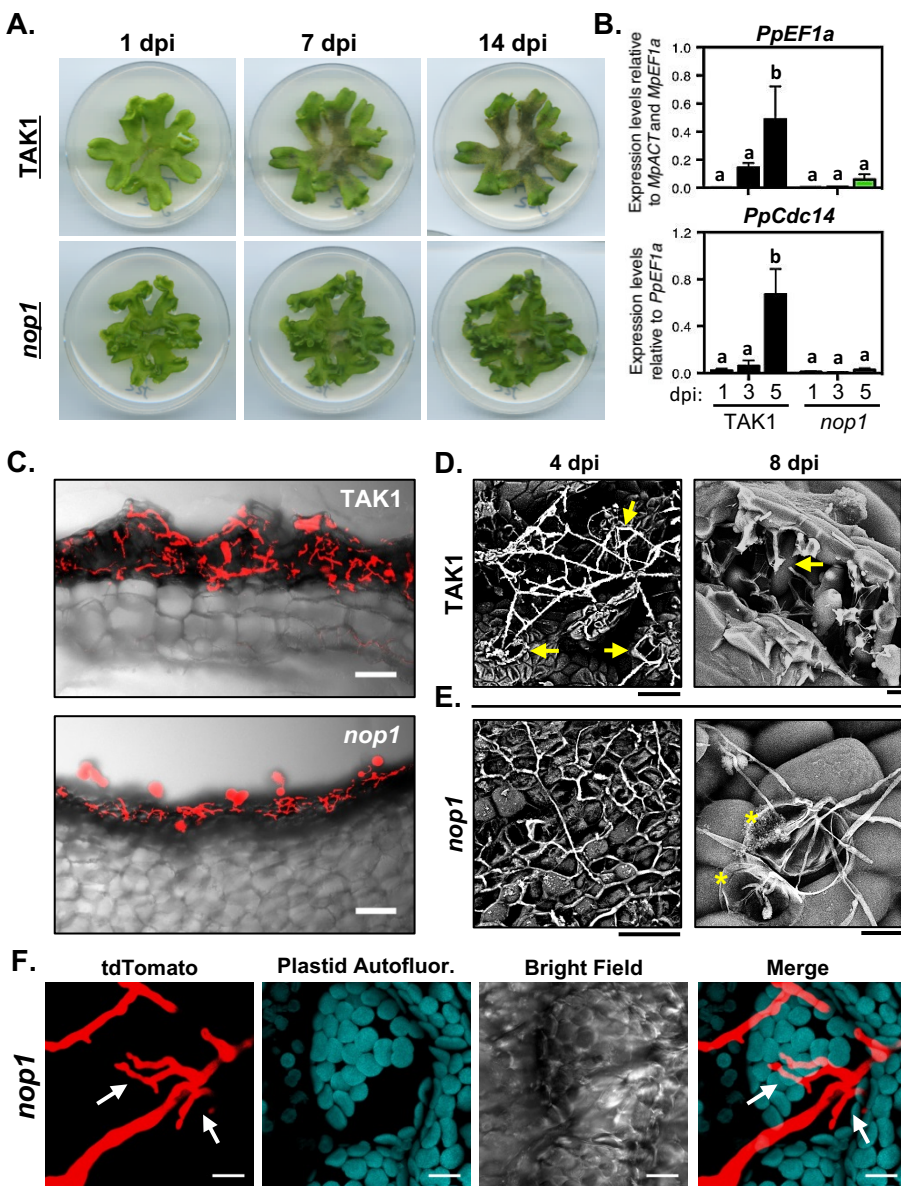


**Fig 5. *Phytophthora palmivora* requires air chambers for the successful colonization of *Marchantia polymorpha* thalli.**

(A) Disease symptoms of 3-week-old *M. polymorpha* TAK1 (wild-type) and *nop1* mutant plants inoculated with *P. palmivora* ARI-td zoospores at 1, 7, and 14 days post inoculation (dpi). (B) Quantification of *P. palmivora* biomass (*PpEF1a*) and sporulation (*PpCdc14*) marker genes during the colonization of wild-type TAK1 and *nop1* plants at 1, 3, and 5 dpi. *PpEF1a* expression was quantified relative to *M. polymorpha* biomass markers (*MpACT* and *MpEF1a*). *PpCdc14* was quantified relative to pathogen biomass (*PpEF1a*). Different letters signify statistically significant differences in transcript abundances (ANOVA, Tukey's HSD  $p < 0.05$ ). (C) Confocal fluorescence microscopy of sectioned TAK1 and *nop1* thalli infected with *P. palmivora* ARI-td at 7 dpi. Micrographs display merged z-stack projections of red pathogen fluorescence and bright field images. Scale bars = 100  $\mu\text{m}$ . (D-E) Cryo-SEM (scanning electron microscopy) of TAK1 and *nop1* thalli infected with *P. palmivora* at 4 or 8 dpi. (D) Micrographs of TAK1 plants demonstrate ARI-td hyphae travelling between air pores (yellow arrows) at 4 dpi and hyphal growth (yellow arrow) within air chambers at 8 dpi. (E) Micrographs of *nop1* plants demonstrate a network of surface hyphae at 4 dpi and collapsed epidermal cells (asterisks) are sometimes observed at 8 dpi. Scale bars = 20  $\mu\text{m}$ . (F) Confocal fluorescence microscopy demonstrating invasive ARI-td hyphal growth in *nop1* epidermal cells at 3 dpi. Micrographs display z-stack projections of red pathogen fluorescence (tdTomato), plastid autofluorescence, bright field images, and tdTomato and plastid fluorescence merged together. Scale bars = 10  $\mu\text{m}$ . Experiments were performed three times (A,B,C,F) or twice (D,E) with similar results.